geosciences

MDPI

Article

Effects of Deviatoric Stress on Macro- and Meso-Mechanical Behavior of Granite for Water-Sealed Caverns Under True Triaxial Loading

Liliang Han [1], Yu Cong [2], Xiaoshan Wang [3,*], Wenyang Du [2], Lixia Zhang [1], Jian Gao [1], Yuming Wang [2] and Zhanchao Zhang [3]

[1] CNPC East China Design Institute Co., Ltd., Qingdao 266000, China; hanliliang-hqc@cnpc.com.cn (L.H.); zhanglixia-hqc@cnpc.com.cn (L.Z.); gaojian03-hqc@cnpc.com.cn (J.G.)
[2] School of Civil Engineering, Qingdao University of Technology, No. 777, Jialingjiang East Road, Qingdao 266520, China; congyu@qut.edu.cn (Y.C.); m15753123211@163.com (W.D.); yum_wdp@163.com (Y.W.)
[3] School of Science, Qingdao University of Technology, No. 777, Jialingjiang East Road, Qingdao 266520, China; zhangzhch@163.com
* Correspondence: wangxiaoshan@qut.edu.cn

Abstract

Based on true triaxial loading experiments and particle flow numerical simulations (PFC3D), this study systematically analyzes the mechanical behavior and failure mechanisms of granite under the influence of stress difference (deviatoric stress). The experimental results indicate that increasing deviatoric stress reduces peak strength, axial strain, and lateral strain, promoting rock failure with less deformation and dilatancy. An energy analysis reveals that higher deviatoric stress suppresses peak energy accumulation, with a greater proportion of energy being dissipated through crack initiation and propagation. Macroscopic observations show that failure surfaces develop combined tensile-shear cracks, evolving into distinct "V" shapes as deviatoric stresses increase. Numerical simulations demonstrate that intermediate principal stress plays a dual role, initially facilitating, then inhibiting, and finally promoting rock failure with its continuous increase. Microscopically, tensile cracks dominate during pre-peak stages, while rapid crack coalescence in the post-peak stage leads to the formation of throughgoing V-shaped failure zones. Particle displacement analysis reveals that deformation concentrates along the minimum principal stress direction, with the displacement vectors ultimately forming a V-shaped boundary that delineates the failure zone. The research provides comprehensive insights into the macro-meso failure characteristics of hard rock under true triaxial conditions, offering valuable guidance for stability prediction and control in underground rock engineering projects such as water-sealed storage caverns.

Keywords: true triaxial test; deviatoric stress; stress–strain curve; energy; cracks

Check for updates

Academic Editor: Mohamed Shahin

Received: 25 November 2025
Revised: 21 January 2026
Accepted: 29 January 2026
Published: 3 February 2026

Copyright: © 2026 by the authors. Licensee MDPI, Basel, Switzerland. This article is an open access article distributed under the terms and conditions of the Creative Commons Attribution (CC BY) license.

1. Introduction

With the rapid development of the global economy, large-scale underground rock engineering projects have proliferated. Among them, water-sealed underground storage caverns have become a key infrastructure for energy storage, owing to their advantages such as a small land footprint, high safety, long service life, and environmental friendliness [1,2]. In China, this technology was first applied in the construction of the Huangdao water-sealed oil cavern; later, it was widely adopted in coastal regions such as Ningbo and

Guangdong [3]. A water-sealed cavern stores oil or gas within hard, intact rock chambers located below a specific water level, where the groundwater pressure in the surrounding rock fractures is maintained at a higher level than that of the internal oil or gas pressure; this effectively prevents leakages and ensures the safety of this energy storage method [4]. The construction and operation of such caverns are often accompanied by various geological hazards, including collapses, rockbursts, water inrush, and roof falls. To address these problems in rock engineering, extensive laboratory studies have been conducted. While theories and findings related to loading paths have become relatively mature and well established, most existing research focuses on aspects such as stress paths and confining pressure combinations [5]. In contrast, the influence of stress difference on the dynamic failure and propagation effects of rocks under true triaxial conditions remains insufficiently explored. Therefore, it is of great practical significance to investigate the mechanical properties of rocks under true triaxial loading conditions and analyze the influence of the stress difference on loading-induced dynamic failure propagation. Such studies can provide valuable guidance for reducing economic losses and enhancing safety during the construction and maintenance of underground engineering projects.

Since Adams and Nicolson (1901) independently developed the first triaxial loading apparatus for rocks [6], many researchers have investigated the failure characteristics of rocks under triaxial stress conditions. With continued advances in manufacturing technologies, Handin et al. (1967) developed a true triaxial loading device [7], marking a milestone in experimental rock mechanics. In recent decades, numerous scholars worldwide have carried out extensive studies on true triaxial loading tests, yielding substantial progress and significant results [8,9]. For example, Zhang et al. [10] conducted triaxial loading tests on red sandstone specimens, using an acoustic emission monitoring system to track energy changes during rock damage and failure. Their results indicate that rock deformation results in axial compression and dilatancy, aligned with the direction of minimum and intermediate principal stresses. Ductility in rock failure becomes more pronounced with increased stress, primarily manifesting as shear failure. Gu et al. [11] conducted a quantitative analysis on the microfabric of five types of granites to elucidate the influence mechanism of microfabric and stress disparity on granite strength. The results show that the strength of granite is primarily determined by the initial damage, the structural coefficient, the biotite content, and the quartz content. With an increase in stress differential, the impact of initial damage and biotite content on granite strength diminishes, while the influence of the quartz content and the structural coefficient on granite strength begins to intensify. Zhang et al. [12] conducted true triaxial creep tests through multistage loading and unloading to describe the creep mechanical behavior of deep hard rocks after stress adjustment. The results show that both σ_1 loading and σ_2 unloading accelerate the creep of granite, while σ_3 unloading promotes the creep in the σ_3 direction; however, the creep in the σ_1 and σ_2 directions was not found to be promoted to any significant extent. Liu et al. [13] carried out true triaxial compression tests on sandstone to examine their energy and damage evolution. Their results reveal that, since the intermediate principal stress exceeds the minimum principal stress, a higher proportion of elastic energy density is induced in that direction, and the damage variable evolves almost linearly during the elastic stage.

Zhang et al. [14] performed a true triaxial compression test and a cyclic loading and unloading test of sandstone specimens under different loads using a self-developed true triaxial disturbance testing system. The findings indicate that the staged cyclic loading and unloading cause the greatest damage to the rock mass, while the staged loading and unloading, with an equal amplitude and an unequal lower limit, cause the least damage to the rock mass. Dong et al. [15] conducted a sandstone mechanical test with different intermediate principal stresses under true triaxial loading, using the rock true triaxial

disturbance unloading test system. The results show that the failure mode of sandstone under true triaxial compression changes from tension-shear composite failure to tension failure. Cao et al. [16] conducted a series of true triaxial monotonic and cyclic loading tests on rough fractured granite. The results show that an increase in the minimum principal stress has a more significant effect on the increase in the peak shear stress of the fractured granite; moreover, they showed that confining pressure is a key factor that limits the fracture slip of fractured granite.

With the limitations of laboratory experiments, an increasing number of researchers have turned to numerical simulations to reproduce rock behavior observed in physical tests. Commonly used methods include finite element software such as ABAQUS and FLAC [17,18], as well as discrete element software such as UDEC and 3DEC [19,20]. Since Cundall (1971) [21–23] proposed the Discrete Element Method (DEM) and developed the Particle Flow Code (PFC), this approach has become a major platform for micromechanical studies of rocks [24,25]. The PFC 5.0 software effectively simulates crack propagation, mechanical behavior, and failure mechanisms within rock materials. Li et al. [26] established two-dimensional models of marble with two parallel fissures and various rock bridge angles, finding that the characteristic strain, stress, and elastic strain energy exhibit various trends with the increment of the rock bridge angle; meanwhile, they observed an increasing trend with the increment of the confining pressure. Li et al. [27] studied the failure characteristics of rockburst specimens, the particle size distribution characteristics of rockburst fragments, and their acoustic emission parameters and rock energy evolution characteristics. The results show that, when the loading rate increases from 1 to 7 kN/s, the peak strain increases gradually, the peak strength increases by 25%, and the specimen expands more significantly in the y-direction. Chen et al. [28] used the SHPB test system, a scanning electron microscope (SEM), and nuclear magnetic resonance (NMR) to look at the compressive strength, fine features, and energy dissipation of rockburst specimens. The study results indicate that 30-day leaching has a significant impact on the nature of the transition. The leaching action will cause changes in the rock's pore erosion and cavity filling.

Kang et al. [29] conducted sets of true triaxial tests on fine-grained and coarse-grained granite specimens featuring arched holes. The results indicate that, under similar loading conditions, the fine-grained granite primarily undergoes slabbing failure without significant flake ejection. In contrast, the coarse-grained granite primarily undergoes rockbursts with particle ejection, and the particle ejection process is relatively continuous over time. Wei et al. [30] conducted discrete element simulations of rock specimens with a pre-existing single flaw under uniaxial compression using the PFC embedded in the "FISH" language. The results indicate that, under uniaxial compression, as the flaw inclination angle increases, the peak stress of the rock continuously decreases, the crack initiation angle and rock propagation stress increase, and the initiation stress of the rock initially decreases and then increases. Yang et al. [31] conducted a true triaxial hydraulic fracturing test and a numerical simulation to study the mechanisms of hydraulic fracture propagation and the rock failure mode of vertical well hydraulic fracturing. The results show that the fracture propagation mode in limestone is mainly divided into two types: single vertical fractures and transverse-longitudinal crossed complex fractures. Li et al. [32] employed the Discrete Element Method to investigate the mechanical behavior and fracture mechanism of marble under true triaxial cyclic loading and unloading, and the results showed that an increase in the intermediate principal stress results in significant deformation anisotropy. The brittle-ductile transformation characteristics are presented with an increase in the minimum principal stress.

In summary, numerous scholars have conducted true triaxial loading experiments to investigate rock failure behavior under various conditions, primarily focusing on the effects of different stress combinations, intermediate principal stresses, and loading paths. However, research on the influence of stress difference on the dynamic failure and propagation effects of rocks under true triaxial conditions remains limited. The goal of this study is to better understand the influence of stress difference on the dynamic loading-failure-propagation behavior of hard rock surrounding underground caverns. Accordingly, we first perform true triaxial loading experiments on granite to analyze the phenomenon from a macroscopic perspective. This is followed by true triaxial numerical simulations to examine it at a microscopic level. In the analysis, we consider deviatoric stress, shear stress, and principal deviatoric stress to evaluate their impact on both static and dynamic failure characteristics in true triaxial tests. From a micromechanical viewpoint, we further explore how stress difference influences the dynamic failure mechanisms that occur during loading.

2. Experimental Methodology

2.1. Specimen Preparation

The granite specimens were taken in situ in Guangdong province, China. The granite was cut into standard cubic specimens with dimensions of 100 mm × 100 mm × 100 mm in accordance with the Standard Test Methods of Engineering Rock Mass. The specimen surfaces were polished to ensure that the unevenness did not exceed 0.02 mm. Some of the specimens are shown in Figure 1. Wave velocity measurements were conducted on the specimens, yielding an average wave velocity of 2940 m/s; the values fluctuated within a 200 m/s range. Based on the elastic stage of the stress–strain curves obtained from uniaxial compression tests, the elastic modulus and Poisson's ratio of the granite were determined as 51.9 GPa and 0.18, respectively.



Figure 1. Sample of granite specimens.

2.2. Experimental Setup

The laboratory experiments were conducted using the true triaxial testing apparatus developed by Chengdu University of Technology (as shown in Figure 2). The machine has a maximum axial load capacity of 3000 kN and a maximum lateral load capacity of 2000 kN, with a force indication error of ±1%. It provides a displacement range of 120 mm and a deformation range of 10 mm. Equipped with a fully rigid loading system and an advanced servo control and data acquisition system, the apparatus enables precise true triaxial loading tests while supporting the real-time recording of stress, strain, and deformation throughout the testing process.

In this experiment, we employed a true triaxial apparatus to conduct the loading tests. A maximum principal stress (σ_1) was applied along the Z-axis; an intermediate principal stress (σ_2) was applied along the Y-axis; a minimum principal stress (σ_3) was applied along the X-axis. The loading path is shown in Figure 3, and the specific experimental scheme is listed in Table 1. The test procedure consisted of three main steps:

(1) Specimen fixation: The horizontal forces along the X and Y directions were increased to 2 kN to secure the specimen laterally.
(2) Confining pressure application: Using displacement control, σ_2 and σ_3 were increased to the target confining stresses at a loading rate of 0.3 mm/min; these were maintained for 5 min to ensure stabilization.
(3) Axial loading: While keeping σ_2 and σ_3 constant, σ_1 was increased at a rate of 0.3 mm/min until the specimen failed.



Figure 2. True triaxial testing apparatus.

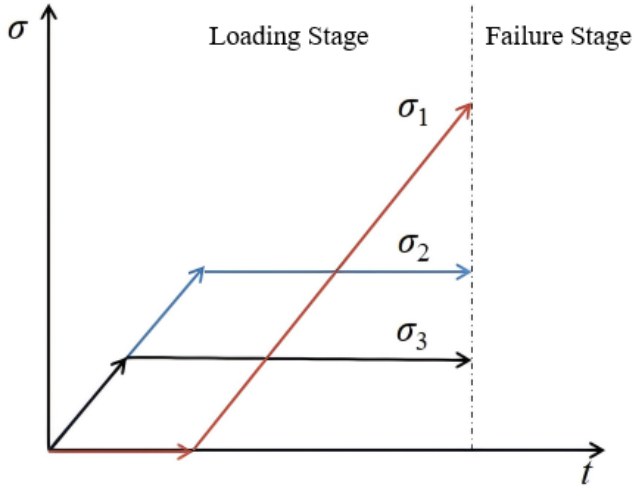
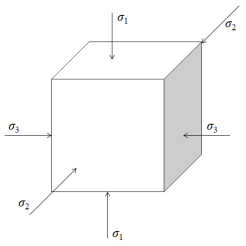


Figure 3. Loading stress path.

Table 1. Loadingtest scheme.

Minimum Principal Stress σ_3/MPa	Intermediate Principal Stress σ_2/MPa	Deviatoric Stress/MPa	Loading Diagram
2	4	2	
4	6	2	
6	8	2	
2	6	4	
6	10	4	
10	14	4	
2	8	6	
8	14	6	

Note: Three specimens were tested for each loading condition.

3. Mechanical Characteristics of Granite Specimens

3.1. Stress–Strain Curve

The axial stress–strain curves from the true triaxial loading tests are shown in Figure 4. ε_1 denotes the strain in the Z direction (axial), ε_2 denotes the strain in the Y direction (σ_2 direction), and ε_3 denotes the strain in the X direction (σ_3 direction). ε_v represents the total volumetric strain, i.e., the sum of the three principal strains, calculated as follows:

$$\varepsilon_v = \varepsilon_1 + \varepsilon_2 + \varepsilon_3 \quad (1)$$

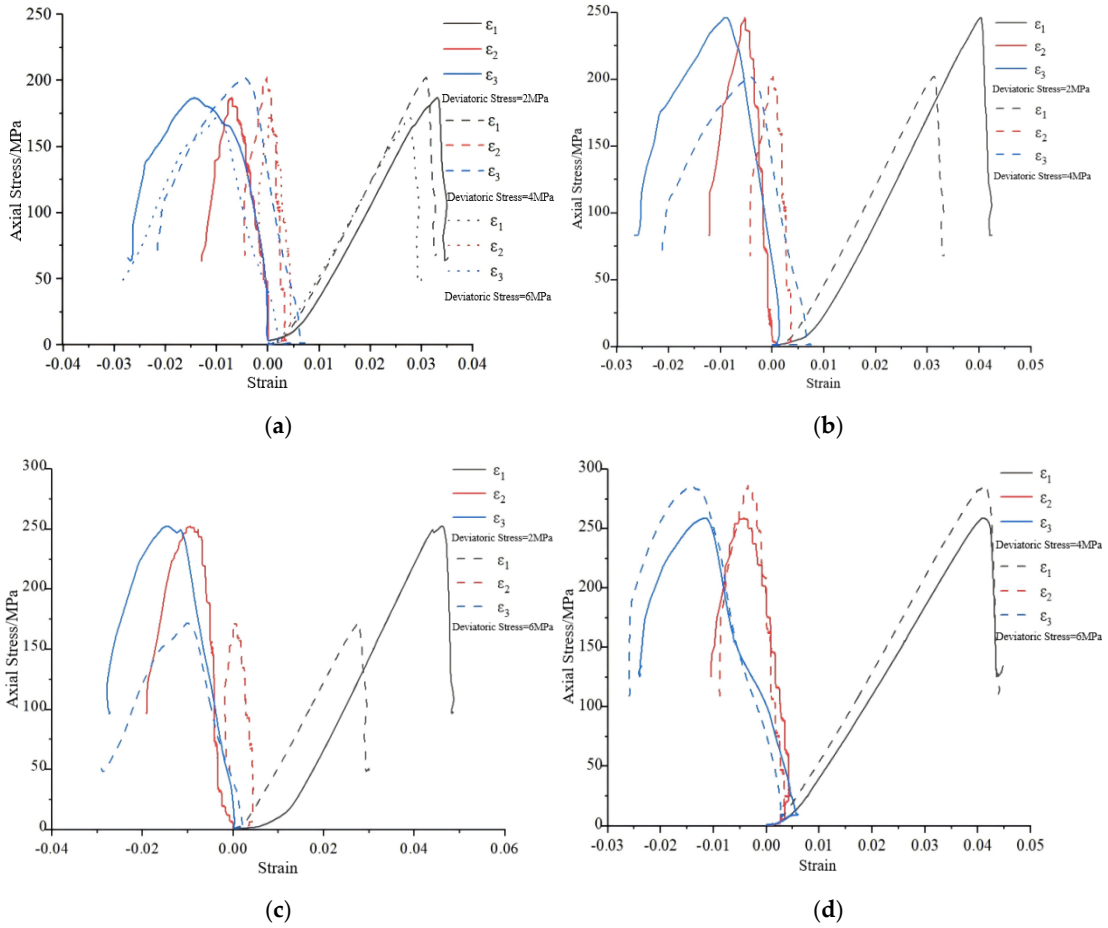


Figure 4. Stress–strain curves of granite specimens under different true triaxial loading conditions. (**a**) σ_3 = 2 MPa; (**b**) σ_3 = 6 MPa; (**c**) σ_2 = 6 MPa; (**d**) σ_2 = 8 MPa.

As shown in Figure 4, at the initial stage, the strain curves are positive: ε_2 and ε_3 evolve in the positive (right-hand) direction, and the crack-induced volumetric strain increases rapidly over a short interval. Under the influence of the confining stresses, the specimen undergoes compression in the X and Y directions; this behavior corresponds to the initial compaction stage.

As the axial stress increases, microcracks begin to develop within the specimen, leading to elastic deformation. The curves of ε_2 and ε_3 shift leftward, indicating a decrease in strain values. The slope of ε_2 is relatively steep, developing almost vertically, while that of ε_3 is gentler. The axial strain ε_1 increases most rapidly, marking this stage as the elastic phase.

As the axial pressure increases and approaches the peak value, cracks within the specimen continuously propagate, resulting in decreasing slopes of the ε_1, ε_2, and ε_3 curves, while the strain values keep increasing. The separation between the ε_2 and ε_3 curves becomes more pronounced, with the strain in the X direction being larger. At this

stage, the slope of ε_v increases and begins to trend rightward, indicating that the specimen undergoes continuous axial compression accompanied by lateral expansion, which is more significant along the minimum principal stress direction. This phase corresponds to the crack propagation stage.

As the test proceeds and the axial stress reaches its peak, the specimen enters the post-peak failure stage. During this stage, internal cracks rapidly expand and coalesce to form a throughgoing failure plane, leading to a sharp drop in axial stress and then to eventual failure. The slopes of the ε_2 and ε_3 curves decrease slightly while their strain values increase, indicating a rapid rise in lateral dilation. At complete failure, the volumetric strain due to cracking approaches zero.

Figure 4 shows the stress–strain curves under different deviatoric stress conditions. When the minimum principal stress (σ_3) is 2 MPa, the peak stress decreases by 8.22%, the Z-direction strain decreases by 14.29%, the Y-direction strain decreases significantly by 92.3%, and the X-direction strain increases by 11.11%. When σ_3 = 6 MPa, the peak stress decreases by 8.73%, the Z-direction strain decreases by 26.53%, the Y-direction strain decreases by 31.58%, and the X-direction strain decreases by 18.52%. With increasing deviatoric stress, both the peak stress and axial strain exhibit a decreasing trend, with the magnitude of reduction becoming more pronounced. The Y-direction strain also decreases, though the rate of reduction becomes smaller.

When the intermediate principal stress (σ_2) is 6 MPa, the peak stress decreases by 17.92%, the Z-direction strain decreases by 21.43%, the Y-direction strain decreases by 66.67%, and the X-direction strain decreases by 18.52%. When σ_2 = 8 MPa, the peak stress decreases by 32.16%, the Z-direction strain decreases by 38.78%, the Y-direction strain decreases sharply by 94.74%, and the X-direction strain decreases by 11.11%. As the deviatoric stress increases, the peak stress, Z-direction strain, and Y-direction strain all show a decreasing trend, with greater declines corresponding to higher deviatoric stress levels. The larger the increase in deviatoric stress, the greater the reduction in both peak stress and strain, indicating that the specimen undergoes smaller deformation and less volumetric expansion in all three directions at failure.

Table 2 presents the peak strain values under different confining pressure conditions in the true triaxial loading tests. ε_1 exhibits the largest value while ε_2 is the smallest. At final failure, the rock undergoes the greatest deformation along the Z direction, with the maximum lateral deformation occurring along the minimum principal stress direction (X).

Table 2. Peak strains under different confining pressure conditions in true triaxial loading tests.

σ_3/MPa	σ_2/MPa	Deviatoric Stress/MPa	ε_1	ε_2	ε_3	ε_v
2	4	2	0.035	−0.013	−0.027	−0.005
4	6	2	0.042	−0.012	−0.027	0.003
6	8	2	0.049	−0.019	−0.027	0.003
2	6	4	0.033	−0.004	−0.022	0.007
2	8	6	0.030	−0.001	−0.030	−0.001

When σ_3 = 2 MPa, as the deviatoric stress increases, both the axial strain and ε_2 (Y-direction strain) decrease, while ε_3 (X-direction strain) first decreases and then increases. The volumetric strain (ε_v) initially increases and then decreases, indicating that the specimen transitions from a dilative state to a compressive state, and finally back to a dilative state at failure.

When σ_2 = 6 MPa and 8 MPa, as the deviatoric stress decreases, both the axial strain and ε_2 increase. For σ_2 = 6 MPa, ε_3 increases while ε_v decreases, suggesting that the

specimen remains in a compressive state. For σ_2 = 8 MPa, ε_3 decreases and ε_v increases, indicating that the specimen transitions from a dilative state to a compressive state.

3.2. Strength Characteristics

Figure 5 shows the peak strength of the granite specimen under different confining pressure conditions in the true triaxial loading tests. The peak stress generally rises, indicating that the higher confining pressure enhances the rock's strength. When the minimum principal stress is σ_3 = 2 MPa, the peak stress first increases and then decreases with the rise in intermediate principal stress, σ_2; this indicates that, at lower σ_2 levels, the intermediate principal stress contributes to strengthening the rock and inhibiting failure, whereas, at higher σ_2 values, it promotes damage and reduces strength. When σ_3 = 6 MPa, the peak stress decreases with increasing σ_2, indicating that the rise in the intermediate principal stress accelerates rock failure.

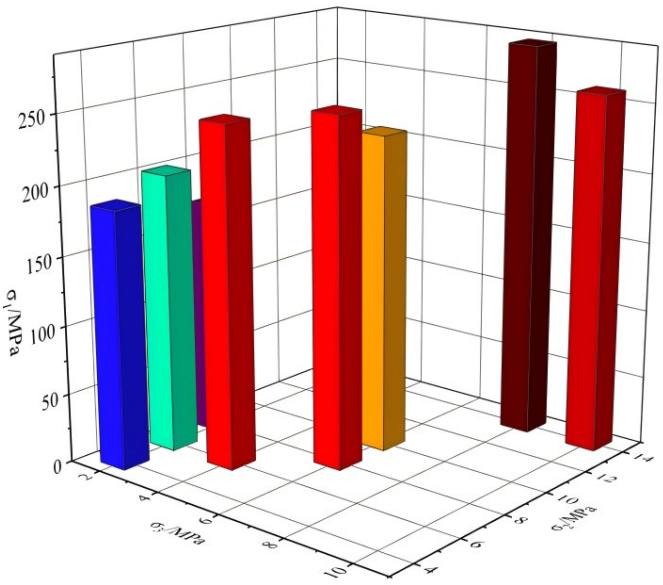


Figure 5. Peak strength of granite specimen under different confining pressures.

When the intermediate principal stress is σ_2 = 6 MPa or 8 MPa, the peak stress increases with the growth of minimum principal stress, σ_3; this demonstrates that higher confining pressure restrains the internal crack propagation and improves the compressive strength. However, when σ_2 = 14 MPa, the peak stress decreases with increasing σ_3, implying that excessive confining pressure facilitates rock failure.

When either the minimum or intermediate principal stress is constant, the peak strength generally decreases with increasing deviatoric stress ($\sigma_2 - \sigma_3$), indicating that greater deviatoric stress promotes rock failure.

3.3. Failure Characteristics

Table 3 presents the macroscopic failure characteristics of the granite specimens under the conducted triaxial loading tests. The cracks were mainly distributed along the σ_2 direction. On the σ_3-oriented surface, the specimens exhibited primarily shear cracks; on the σ_2-oriented surface, the specimens showed dominant shear cracks with a few tensile cracks, accompanied by minor spalling and rock debris on the surface. As the axial load increased, internal cracks developed progressively, with most propagating along the σ_2 direction, forming throughgoing cracks that eventually led to specimen failure.

Table 3. Macroscopic failure characteristics in true triaxial loading tests.

σ_3 (*X*-Axis) /MPa	σ_2 (*Y*-Axis) /MPa	Deviatoric Stress/MPa	Along σ_3 Direction	Along σ_2 Direction
2	4	2		
2	6	4		
2	8	6		

Under different deviatoric stress levels, the crack evolution exhibited distinct characteristics. When the deviatoric stress was 2 MPa, cracks along the σ_2 direction mainly propagated vertically, and splitting cracks appeared on the left side of the σ_3-oriented surface. When the deviatoric stress was 4 MPa, the number of cracks along the σ_2 direction increased and gradually inclined; the specimen surface exhibited tensile, shear, and splitting cracks, with numerous fine cracks and partial surface spalling, while the σ_3-oriented surface contained more cracks that did not fully develop into open fractures. When the deviatoric stress reached 6 MPa, the number and inclination of throughgoing cracks along the σ_2 direction further increased, and splitting cracks formed on the right side. The cracks along both the σ_2 and σ_3 directions displayed a characteristic V-shaped failure pattern. With increasing deviatoric stress, the number of throughgoing cracks progressively increased, and their inclination became more pronounced, gradually transitioning toward a V-shaped failure mode.

3.4. Energy Evolution Characteristics

Assuming that no energy is exchanged with the surroundings during the loading process, the work performed by the testing machine on the specimen is denoted by U. By

the law of energy conservation, the energy absorbed by the specimen under the true-triaxial stress path can be expressed as follows:

$$U = \int \sigma_1 d\varepsilon_1 + \int \sigma_2 d\varepsilon_2 + \int \sigma_3 d\varepsilon_3 \quad (2)$$

Among these, U_1 represents the energy absorbed by the specimen due to axial deformation under the action of σ_1; U_2 represents the energy absorbed due to lateral deformation under σ_2; and U_3 represents the energy absorbed due to lateral deformation under σ_3.

In addition, when the specimen deforms under the external forces applied by the testing machine, the absorbed energy can be divided into two parts: one part is dissipated energy (U_d), which is consumed by the initiation and propagation of microcracks as well as the formation of macroscopic fractures; the other part is elastic strain energy (U_e), which is stored in the specimen as elastic deformation. Therefore, the total absorbed energy of the specimen can be expressed as follows:

$$U = U_d + U_e \quad (3)$$

The elastic strain energy can be specifically expressed as follows:

$$U_e \approx \frac{1}{2E}\left[\sigma_1^2 + \sigma_2^2 + \sigma_3^2 - 2v(\sigma_1\sigma_2 + \sigma_1\sigma_3 + \sigma_2\sigma_3)\right] \quad (4)$$

Here, E denotes the elastic modulus, and υ represents Poisson's ratio, both determined from the elastic stage of the true triaxial loading tests.

During the true triaxial loading test, the energy–stress–strain curves were obtained. Taking the loading rate of 0.3 mm/min, with σ_3 = 2 MPa and σ_2 = 4 MPa as an example, the results are shown in Figure 6. The dissipated energy exhibits a power-law-type acceleration with increasing axial strain prior to failure. This behavior is consistent with the physical characteristics of failure precursors described by the time-reversed Omori law, where damage accumulation accelerates as the system approaches instability.

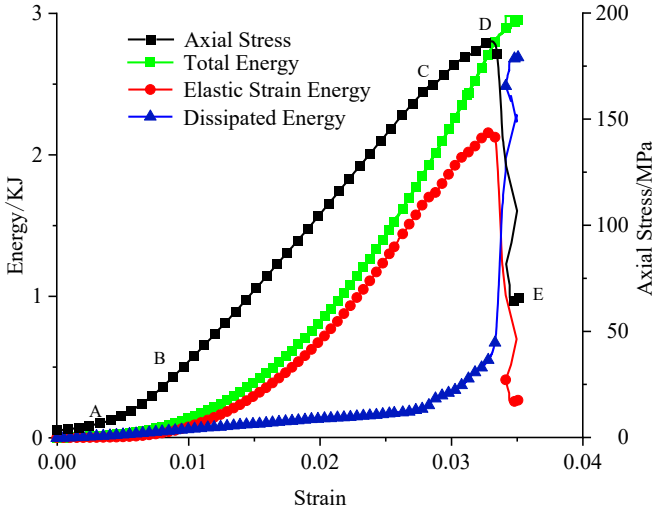


Figure 6. Energy–stress–strain curves during true triaxial loading testing of hard rock.

In the AB stage, the specimen absorbs only a small amount of energy, and all energy components show minimal variation. This stage corresponds to the initial compaction phase, during which the absorbed energy is mainly used to close pre-existing microcracks within the specimen. In the BC stage, representing the elastic stage, both the total energy and elastic strain energy continuously increase, while the dissipated energy grows slowly.

Most of the absorbed energy during this stage is stored as elastic deformation. In the CD stage, the growth rate of elastic strain energy slows down, whereas the dissipated energy increases more rapidly, indicating the initiation and propagation of internal cracks within the specimen. In the DE stage, the axial stress exceeds the peak strength, leading to a sharp decrease in elastic strain energy and a rapid increase in dissipated energy. In this stage, the intense failure of the specimen can be observed, during which the cracks within the specimen expand rapidly, resulting in catastrophic fracture.

Table 4 presents the peak energy values under different confining pressures. When σ_3 = 2 MPa, the energy first increases and then decreases with the rise in deviatoric stress. The total energy changes by +2.71% and −21.78%, while the dissipated energy changes by +1.86% and −18.61%, respectively. When σ_3 = 6 MPa, all forms of energy decrease as deviatoric stress increases, with the total energy decreasing by 17.86% and the dissipated energy by 16.08%.

Table 4. Energy peaks under different confining pressures.

σ_3/MPa	σ_2/MPa	Deviatoric Stress/MPa	Total Energy Peak/KJ·m^3	Dissipated Energy Peak/KJ·m^3	Proportion of Dissipated Energy
2	4	2	2.95	2.69	91.19%
2	6	4	3.03	2.74	90.43%
2	8	6	2.37	2.23	94.09%
4	6	2	4.28	3.86	90.19%
6	8	2	4.87	4.29	88.09%
6	10	4	4.00	3.60	90.00%

Similarly, when σ_2 = 6 MPa and σ_2 = 8 MPa, all energy components decrease with increasing deviatoric stress. Specifically, at σ_2 = 6 MPa, the total energy decreases by 29.21%, and the dissipated energy decreases by 29.02%; at σ_2 = 8 MPa, the total energy decreases by 51.33%, and the dissipated energy decreases by 48.02%.

The proportion of dissipated energy represents the ratio of dissipated energy to total energy at the point of specimen failure. When σ_3 or σ_2 is constant, the proportion of dissipated energy increases with rising deviatoric stress. Although both total energy and dissipated energy values decrease, the relative proportion of dissipated energy grows, indicating that a larger fraction of the total energy is consumed in crack initiation and propagation after failure.

4. Influence of Stress Difference on True Triaxial Loading Failure

4.1. Establishment of the Particle Flow Model

The PFC program effectively captures the microscopic structural characteristics of rock materials. The key to accurate simulation lies in the selection and calibration of model parameters, which must be verified through multiple iterations to ensure the model's reliability. The modeling process for the particle flow numerical simulation is outlined here.

Defining the boundary and generating particles: The boundary range is determined according to the actual dimensions of the rock specimen, defining the size of the "walls". Within the walls, particles of varying radii are generated using the ball command and are evenly distributed to form the specimen. Figure 7 shows the initial particle flow model. Loading is achieved by controlling the movement of the walls at a specified velocity. The model is validated by comparing the numerical results with laboratory test results, such as stress–strain curves and failure patterns. The parallel bond model is selected for simulating rock materials, as it can more accurately represent their mechanical behavior and fracture characteristics.

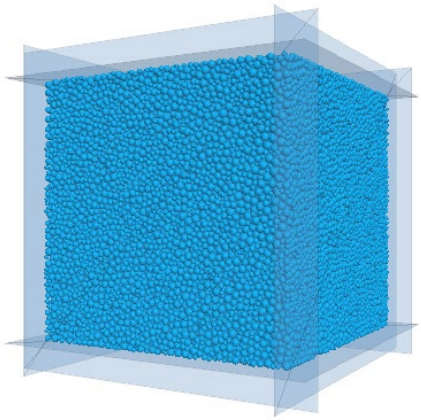


Figure 7. Initial particle flow model.

4.2. Calibration of Micromechanical Parameters

At present, the mainstream approach is to adjust the micromechanical parameters through a trial-and-error method, matching the results of laboratory experiments with those of numerical simulations. In this study, based on laboratory test results, a set of preliminary parameters was established. Through extensive data fitting and iterative calibration, a reliable set of micromechanical parameters for the granite particle flow simulation was finally obtained, as shown in Table 5.

Table 5. Micromechanical parameters of the numerical model.

Particle–Particle Contact Modulus E_c/GPa	Particle Stiffness Ratio k_n/k_s	Parallel-Bond Elastic Modulus $\overline{E}_c$/Gpa	Parallel-Bond Stiffness Ratio $\overline{k}_n/\overline{k}_s$	Particle Friction Coefficient μ	Parallel-Bond Radius Multiplier $\overline{\lambda}$	Mean Normal Strength of Parallel Bonds $\overline{\sigma}_c$/Mpa	Standard Deviation of Normal Strength of Parallel Bonds $\overline{\sigma}_{cs}$/Mpa	Mean Shear Strength of Parallel Bonds $\overline{\tau}_c$/Mpa	Standard Deviation of Shear Strength of Parallel Bonds $\overline{\tau}_{cs}$/Mpa
8.5	6	8.5	6	0.5	0.7	130	5	70	0

The comparison between the laboratory test curve and the numerical simulation curve is shown in Figure 8. The stress–strain curves exhibit good overall agreement, with close correspondence in terms of peak stress, corresponding strain, and loading points, indicating a high level of consistency between the numerical simulation and the laboratory results. Since PFC3D performs an initial equilibrium adjustment before loading—ensuring uniform particle distribution within the model—the initial compaction stage is not prominently observed.

The comparison between the macroscopic failure patterns observed in the laboratory tests and those from the numerical simulations is shown in Figure 9. In the numerical simulation, blue indicates tensile cracks, while red represents shear cracks. It can be observed that the simulated failure mode closely matches that of the laboratory tests, with several through-going cracks occurring in similar locations. It is demonstrated that the selected set of micromechanical parameters can accurately capture the mechanical behavior and failure characteristics of hard rock.

By comparing the stress–strain curves, peak stresses, loading points, and failure characteristics obtained from the laboratory and numerical simulation tests, it is confirmed that the micromechanical parameters listed in Table 5 can effectively reproduce the macroscopic behavior of granite under true triaxial loading conditions. Subsequent analyses and simulations in this study are therefore conducted based on these calibrated parameters.

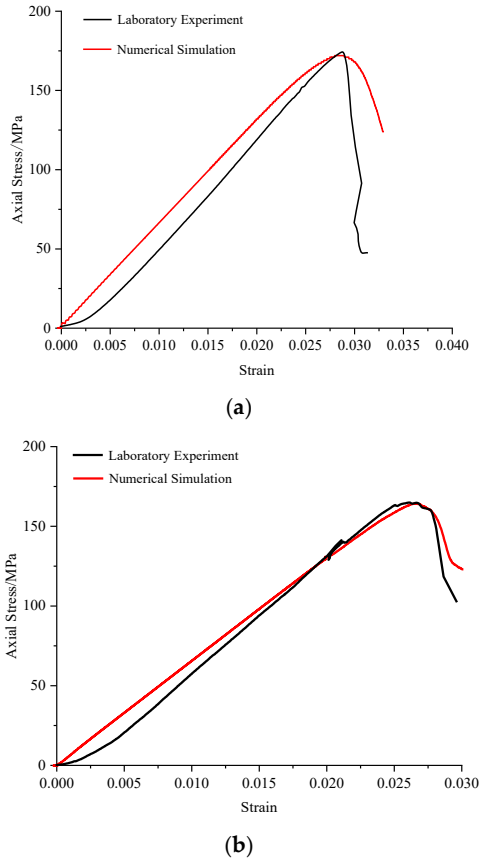


Figure 8. Comparison between laboratory test curves and numerical simulation curves. (**a**) Comparison of stress–strain curves under true triaxial loading. (**b**) Comparison of stress–strain curves under true triaxial axial loading and confining pressure loading.

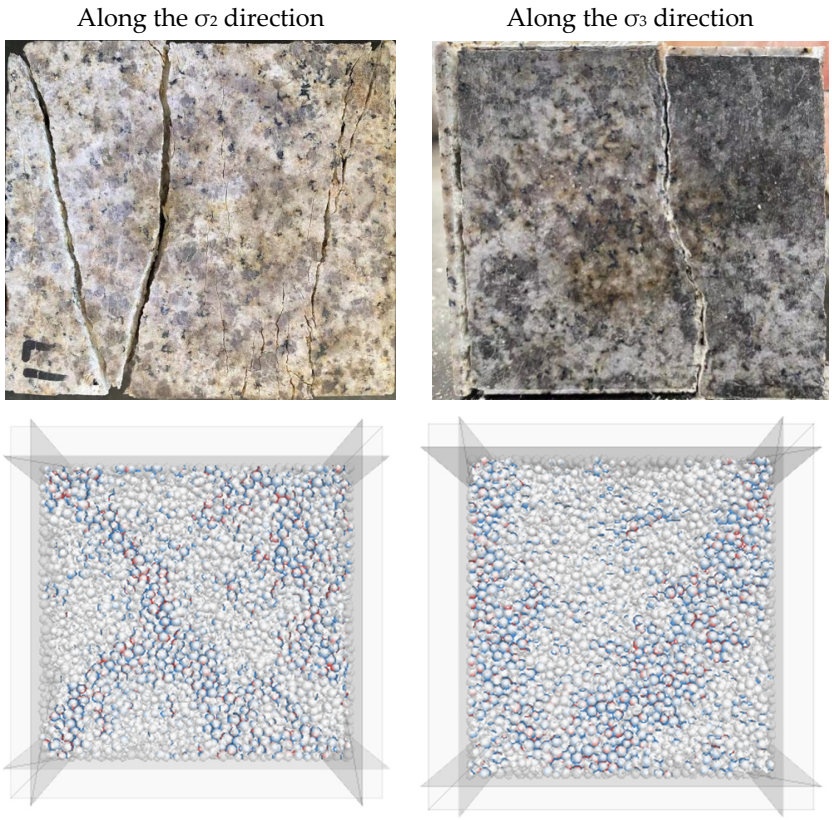


Figure 9. Comparison of failure modes between laboratory tests and numerical simulations.

4.3. Experimental Cases

Based on the loading paths from indoor tests, numerical simulations were conducted. The numerical simulation process for the true triaxial loading tests was conducted as follows:

(1) Model setup: Model dimensions were determined using the "wall," with consistent dimensions for granite specimens. 'Spheres' with diameters ranging from 2.25 to 3.25 mm were generated within the "wall," and servo control was used to achieve balanced and uniform particle distribution.
(2) Increasing confining pressure: The "wall" was moved via servo control to increments σ_2 and σ_3 at the same rate as the target stress (as shown in Table 6).
(3) Increasing axial load: σ_2 and σ_3 were held constant while incrementing σ_1 at a rate of 0.0025 MPa/step until specimen failure occurred.

Table 6. Numerical simulation test plan for true triaxial loading.

Minimum Principal Stress σ_3/MPa	Median Principal Stress σ_2/MPa
2	4, 6, 8, 10, 12
6	8, 10, 12, 14, 16
10	12, 14, 16, 18, 20

5. Micro-Scale Characteristics of True Triaxial Loading Failure

5.1. Characteristics of Stress–Strain Curves

Figure 10 shows the stress–strain curves under the influence of the minimum principal stress when σ_2 = 10 MPa. At final failure, ε_3 exhibits the largest value, indicating significant dilatation along the X direction. The peak stress shows only minor variation, fluctuating within the range of 166–169.6 MPa. As the peak stress increases, ε_3 decreases, while ε_1 and ε_2 increase correspondingly.

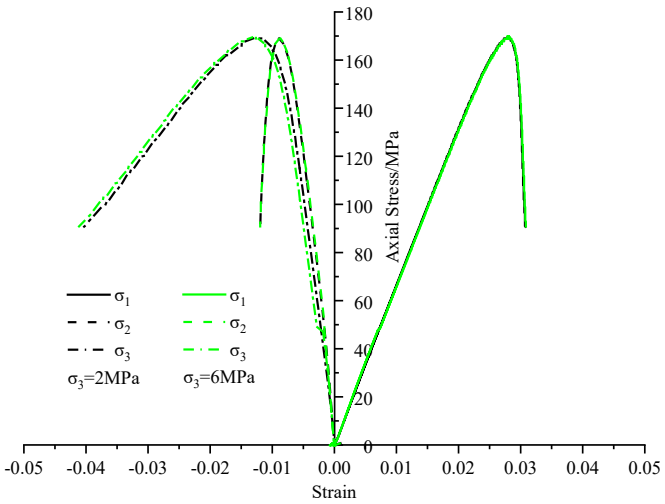


Figure 10. Stress–strain curves of granite under different minimum principal stresses at σ_2 = 10 MPa.

Figure 11 presents the stress–strain curves that were observed under the influence of the intermediate principal stress when σ_3 = 2 MPa. The overall variation trends of the curves are generally consistent. As the intermediate principal stress increases, the peak stress gradually rises. At final failure, ε_1 shows little variation, with a slight increasing trend; ε_2 gradually decreases, and ε_3 gradually increases. These findings indicate that dilatation in the X and Z directions becomes more pronounced, while compression in the Y direction intensifies.

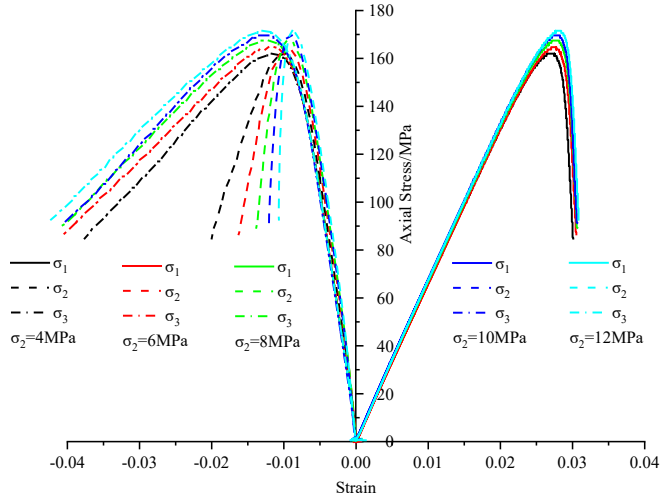


Figure 11. Stress–strain curves of granite under different intermediate principal stresses at σ_3 = 2 MPa.

Table 7 presents the peak stresses obtained from particle flow simulations under true triaxial loading conditions. Under the influence of the minimum principal stress, peak stress generally exhibits an initial decrease followed by an increasing trend. As the minimum principal stress increases, this increasing trend gradually moderates. When the minimum principal stress (σ_3) is held constant, the peak stress demonstrates an overall increasing trend with the rise in deviatoric stress. The most significant increase of 5.62% occurs at σ_3 = 2 MPa, while the maximum increase is only 1.73% at σ_3 = 6 MPa.

Table 7. Peak stresses from true triaxial loading particle flow simulations.

Minimum Principal Stress σ_3/MPa	Intermediate Principal Stress σ_2/MPa	Deviatoric Stress/MPa	Peak Stress/MPa
2	4	2	162
	6	4	165
	8	6	167
	10	8	169.4
	12	10	171.1
6	8	2	167.6
	10	4	169.6
	12	6	167.6
	14	8	169.4
	16	10	170.5
10	12	2	167.8
	14	4	173
	16	6	170.7
	18	8	172.1
	20	10	173

Under the influence of the intermediate principal stress, with a minimum principal stress of 2 MPa, the peak stress shows an increasing trend as the intermediate principal stress increases. However, at minimum principal stress levels of 4, 6, 8, and 10 MPa, the peak stress displays a pattern of an initial increase, followed by a decrease, and then a subsequent increase. This indicates that the intermediate principal stress initially facilitates rock failure, then inhibits it, and ultimately promotes rock failure again with its continued increase.

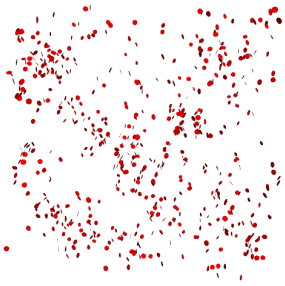
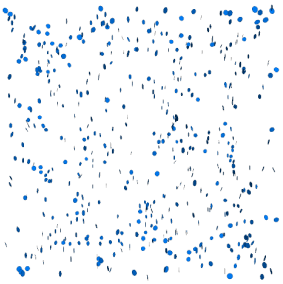
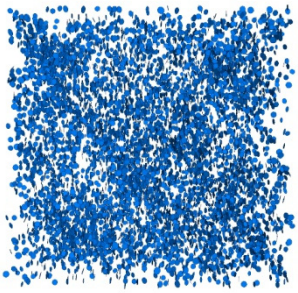
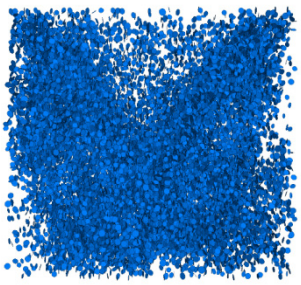
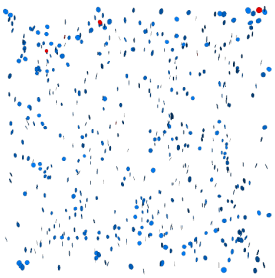
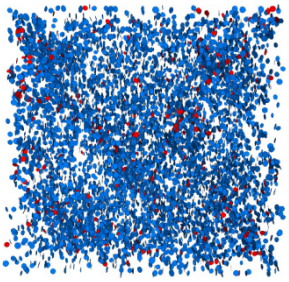
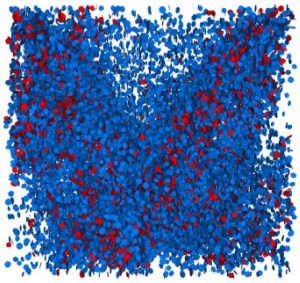
5.2. Microcrack Characteristics

PFC3D software was used to effectively capture the internal crack evolution within the specimen and to record the complete process of crack development during loading.

Table 8 presents the mesoscopic crack evolution process from the particle flow simulation under true triaxial loading. In the table, blue indicates tensile failures, while red represents shear failures. The tensile cracks (blue) are greater in number and more

widely distributed, playing a predominant role in the failure mechanism under true triaxial loading conditions.

Table 8. Microscopic evolution diagrams from true triaxial loading particle flow simulations.

	Pre-Peak Stage	Peak Stage	Post-Peak Stage
Shear Cracks			
Tensile Cracks			
Total Cracks			

During the pre-peak stage, microcracks begin to initiate and develop at a slow rate. Shear cracks are few in number and sporadically distributed in the upper part of the specimen, while tensile cracks are dispersed throughout the entire sample. As the load continuously increases towards the peak stage, the number of cracks grows significantly. At this point, tensile cracks fully permeate the specimen and, together with shear cracks, coalesce to form distinct failure zones. In the post-peak stage, the specimen's load-bearing capacity drops abruptly, accompanied by a rapid increase in crack population. This ultimately leads to the formation of a through-going failure surface, with fractures propagating along a specific inclination in the Z-direction.

Table 9 presents the failure characteristics that were observed under different intermediate principal stresses. At an intermediate principal stress of 4 MPa, failures are dispersed throughout the specimen. As the intermediate principal stress increases, the specimen ultimately develops a more pronounced V-shaped failure pattern, with a reduction in crack distribution on both sides and the central top region.

Table 10 presents the failure characteristics under different minimum principal stresses. All modes are similar, exhibiting distinct "V" cracks. As the minimum principal stress increases, its influence becomes more pronounced: the initiation point at the base of the V-shaped crack shifts leftward, while the crack distribution on the right side and the central top region of the specimen decreases.

Table 9. Failure characteristics corresponding to different intermediate principal stresses at σ_3 = 2 MPa.

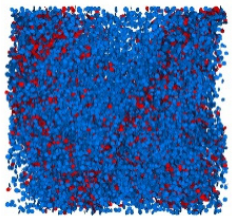
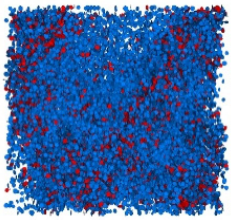
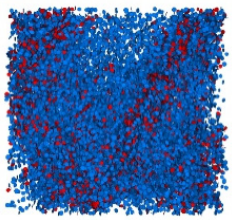
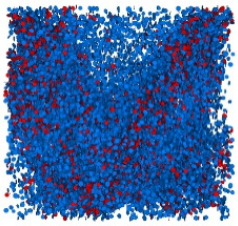
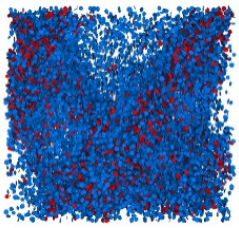
σ_2 = 4 MPa	σ_2 = 6 MPa	σ_2 = 8 MPa	σ_2 = 10 MPa	σ_2 = 12 MPa
				

Table 10. Failure characteristics corresponding to different minimum principal stresses at σ_2 = 10 MPa.

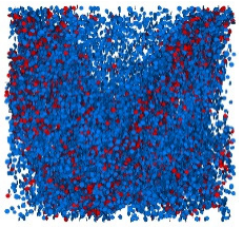
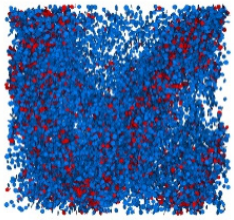
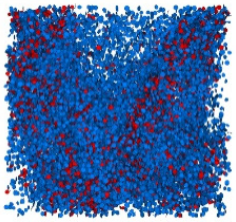
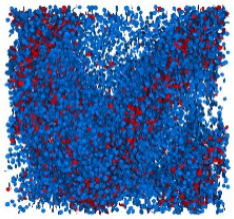
σ_3 = 2 MPa	σ_3 = 4 MPa	σ_3 = 6 MPa	σ_3 = 8 MPa
			

Figure 12 illustrates the crack evolution process under different intermediate principal stress conditions while maintaining a constant minimum principal stress of 2 MPa. Crack development is predominantly concentrated in the post-peak failure stage. Upon entering this stage, cracks propagate rapidly, with all cracks following a similar evolutionary process. As the deviatoric stress increases, the total number of cracks at the final failure stage (defined as 50% of the post-peak strength) gradually decreases. Concurrently, the corresponding axial strain increases, indicating a more pronounced brittle failure characteristic. The rapid increase in the total number of cracks reflects an intensified microcrack coalescence process, which may serve as an effective indicator of imminent macroscopic failure.

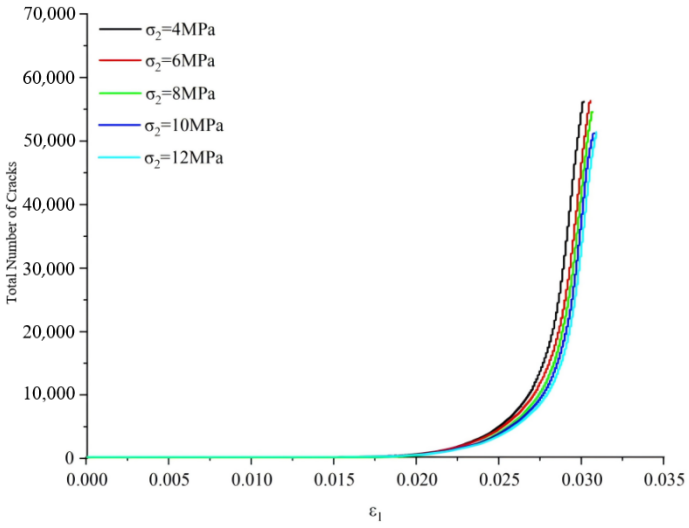
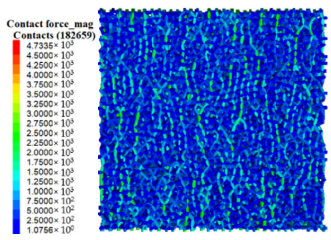
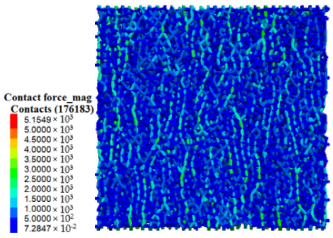
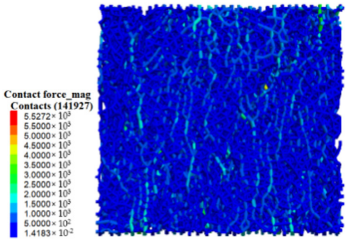


Figure 12. Relationship between axial strain (ε_1) and crack evolution.

5.3. Mesoscopic Force Field Evolution Characteristics

Table 11 illustrates the evolution characteristics of the mesoscopic force field formed by interconnected contact force chains, where the thickness of each force chain is proportional to the magnitude of the contact force. During the pre-peak stage, the contact force chains are uniformly distributed throughout the specimen, with relatively small contact forces, indicating minimal internal damage and a well-preserved structural integrity. As the load continues to increase and reaches the peak stress, the distribution of contact force chains becomes more localized, and the gaps between individual force chains widen. At the post-peak 50% state, some force chains near the specimen boundaries either disappear or become thinner. Following specimen failure, the load-bearing capacity drops abruptly, resulting in a reduction in contact forces generated through wall compression. With further loading, the rupture of parallel bonds leads to a decrease in contact forces, or the relative displacement between particles causes the complete loss of contact forces.

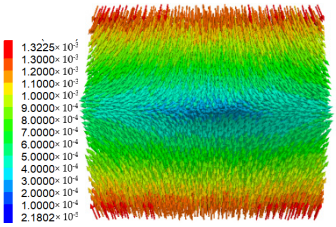
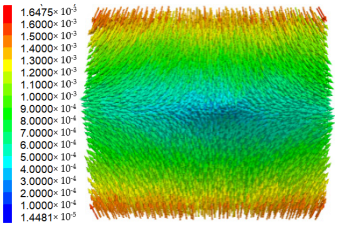
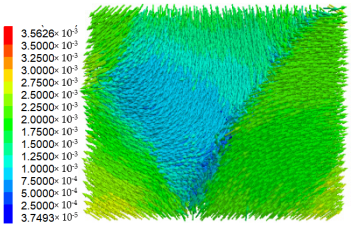
Table 11. Evolution characteristics of the mesoscopic force field.

Pre-Peak Stage	Peak Stage	Post-Peak Stage
		

5.4. Particle Displacement Vector Field Characteristics

The macroscopic deformation of a specimen under load is determined by the internal particle displacements. The characteristics of the particle displacement vector field effectively reveal the mechanisms underlying rock deformation and failure. Table 12 illustrates the evolution of the particle displacement vector field, where arrows represent the displacement vectors of individual particles.

Table 12. Evolution characteristics of the particle displacement vector field.

Pre-Peak Stage	Peak Stage	Post-Peak Stage
		

During the pre-peak stage, as the axial (Z-direction) load increases, the largest displacements occur at the top and bottom ends of the specimen. Most arrows point in the direction of the minimum principal stress. Along the *Z*-axis, from the ends toward the center, the displacement magnitude decreases, as indicated by a color gradient from red to blue. Since the minimum principal stress is lower than the intermediate principal stress, particle displacement arrows show a greater tendency to develop in the X-direction.

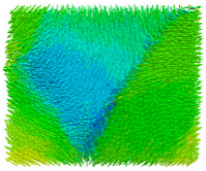
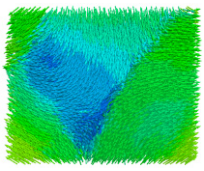
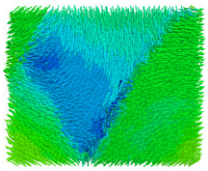
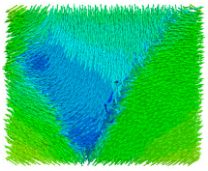
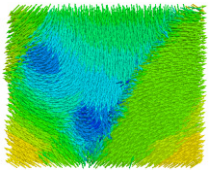
As the load continues to rise and reaches the peak stage, the red high-displacement zones at the upper and lower ends shrink, indicating reduced particle displacement in

these regions. Meanwhile, the blue low-displacement area in the center expands. While the Y-direction displacement remains relatively small, the X-direction displacement increases, causing the middle of both sides of the specimen to bulge outward. This pattern demonstrates that compressive deformation is primarily developing in the X-direction.

In the post-peak stage, the specimen undergoes complete failure. The displacement vectors form a distinct V-shaped boundary. On the right side, most vectors point to the right, whereas on the left side, they predominantly point toward the middle of the left boundary. The maximum displacements are concentrated at the bottom left and right corners of the specimen.

Table 13 presents the characteristics of the particle displacement vector field under the influence of the intermediate principal stress. After complete failure, the specimen develops a V-shaped failure surface. As the intermediate principal stress increases, the particle displacements generally exhibit an increasing trend. The relative displacement at the bottom of the V-shaped failure zone decreases, while the particle displacements at the two bottom corners increase. With the rise in intermediate principal stress, the particle displacements on the inner side of the V-shaped zone relatively decrease, whereas those on the outer side increase, leading to an overall enlargement of the macroscopic deformation of the model.

Table 13. Characteristics of particle displacement vector under the influence of intermediate principal stress.

σ_2 = 4 MPa	σ_2 = 6 MPa	σ_2 = 8 MPa	σ_2 = 10 MPa	σ_2 = 12 MPa
				

6. Conclusions

In this study, we conducted true triaxial loading tests on granite using a true triaxial servo-controlled system; moreover, we comparatively analyzed the macroscopic characteristics under the influence of deviatoric stress, including mechanical properties, deformation and failure behavior, and energy evolution. Numerical simulations were subsequently performed using the Particle Flow Code (PFC3D, enabling a comparative examination of the mesoscopic characteristics during the failure process of granite under stress difference, such as the evolution of the force field, crack development, and particle displacement vector field. The main conclusions are summarized as follows:

(1) Under true triaxial loading conditions, as the deviatoric stress increases, the peak stress, Z-direction strain, and Y-direction strain exhibit decreasing trends with growing reduction magnitudes. A larger increment in deviatoric stress leads to smaller specimen deformation and reduced dilatancy at failure, indicating that increased deviatoric stress promotes rock failure.

(2) When either the minimum principal stress or the intermediate principal stress is held constant, an increase in deviatoric stress suppresses the generation of peak energy. After specimen failure, a larger portion of the total energy is utilized for crack initiation and propagation.

(3) The specimen surface displays fractures that are formed by the combined action of tension and shear, along with fine microcracks. As the deviatoric stress increases, the

number of interconnected cracks rises, and the inclination angle of the cracks grows, gradually transitioning toward a V-shaped pattern.

(4) The intermediate principal stress initially facilitates rock failure, then inhibits it, and ultimately promotes failure again with its continued increase. In the true triaxial numerical simulations, crack development during the pre-peak stage progresses slowly. Shear cracks are sporadically and randomly distributed throughout the specimen, whereas tensile cracks extensively permeate the sample. During the post-peak stage, cracks propagate rapidly, coalescing into a distinct V-shaped crack pattern. As the intermediate principal stress increases, this failure pattern becomes more pronounced.

(5) In the pre-peak stage of the true triaxial simulation, the largest displacements occur at the top and bottom ends of the specimen, oriented in the direction of the minimum principal stress. The circumferential particle displacements show a predominant development in the X-direction. In the post-peak stage, the Z-direction displacement variation decreases while the X-direction displacement increases, causing the middle section of both sides of the specimen to bulge outward. This indicates that compressive deformation primarily develops along the X-direction. Ultimately, the displacement vectors form a V-shaped boundary, delineating the failure zone.

Despite the valuable insights obtained from this study, several issues deserve further investigation. First, future experiments should incorporate a larger number of specimens and different rock types to quantitatively evaluate the statistical robustness and material dependency of the observed energy evolution and failure characteristics.

Second, combining true triaxial testing with high-resolution acoustic emission monitoring and numerical modeling would be beneficial for developing quantitative failure forecasting models based on energy and damage precursors.

Third, extending the findings to deep underground engineering, such as water-sealed caverns.

Author Contributions: Conceptualization: X.W. and Y.C.; Methodology: X.W. and Y.C.; Investigation: L.H., L.Z. and Z.Z.; Data curation: W.D., Y.W. and Z.Z.; Formal analysis: W.D. and Y.W.; Writing—original draft: L.H. and L.Z.; Writing—review and editing: J.G. and X.W.; Supervision: J.G. All authors have read and agreed to the published version of the manuscript.

Funding: This research was financially supported by the National Natural Science Foundation of China under Grant Nos. 42207201, 52179204. This work is also supported by the Open Project Fund of the Engineering Research Center of Concrete Technology under Marine Environment, Ministry of Education, Qingdao University of Technology (CK-2024-0016).

Data Availability Statement: The raw data supporting the conclusions of this article will be made available by the authors on request.

Conflicts of Interest: Authors Liliang Han, Lixia Zhang and Jian Gao were employed by the company CNPC East China Design Institute Co., Ltd. The remaining authors declare that the research was conducted in the absence of any commercial or financial relationships that could be construed as a potential conflict of interest.

References

1. Li, W.; Hong, C.; Qiao, L.; Ma, J.; Peng, Z.; Wang, Z. Reliability analysis of underground water-sealed storage caverns stability: Method and application. *Tunn. Undergr. Space Technol.* **2025**, *161*, 106550. [CrossRef]
2. Xue, Y.; Ning, Z.; Kong, F.; Qiu, D.; Liu, Y.; Jiang, X. Water-sealing performance assessment of the water curtain system in underground water-sealed oil-storage caverns. *Environ. Earth Sci.* **2022**, *81*, 172. [CrossRef]
3. Li, Z.; Xue, Y.; Li, S.; Qiu, D.; Su, M.; Zhao, Y.; Zhou, B. An analytical model for surrounding rock classification during underground water-sealed caverns construction: A case study from eastern China. *Environ. Earth Sci.* **2019**, *78*, 602. [CrossRef]

4. Duan, B.F.; Xia, H.L.; Yang, X.X. Impacts of bench blasting vibration on the stability of the surrounding rock masses of roadways. *Tunn. Undergr. Space Technol.* **2018**, *71*, 605–622. [CrossRef]
5. Feng, X.T.; Xu, H.; Yang, C.; Zhang, X.; Gao, Y. Influence of Loading and Unloading Stress Paths on the Deformation and Failure Features of Jinping Marble Under True Triaxial Compression. *Rock Mech. Rock Eng.* **2022**, *7*, 3287–3301. [CrossRef]
6. Bezalel, H.; Kiyoo, M. *Experimental Rock Mechanics 2007 Taylor & Francis London*; CRC Press: London, UK, 2007; Volume 44.
7. Haimson, B.; Chang, C. A new true triaxial cell for testing mechanical properties of rock, and its use to determine rock strength and deformability of Westerly granite. *Int. J. Rock Mech. Min. Sci.* **2000**, *37*, 285–296. [CrossRef]
8. Poorsolhjouy, P.; Mews, S.K.; Misra, A. Rock Failure Characteristics Evaluated Under True Triaxial Loading from Micro-mechanical Viewpoint. *Rock Mech. Rock Eng.* **2025**, *58*, 5653–5672. [CrossRef]
9. Meng, F.; Yue, Z.; Zhou, X.; Song, J.; Ma, X.; Hu, D.; Zhou, H.; Guo, T. Fracture Slip Behavior in Granite Under High-Temperature True Triaxial Loading Tests. *Rock Mech. Rock Eng.* **2024**, *57*, 9669–9694. [CrossRef]
10. Zhang, S.C.; Song, S.L.; Han, X.X. Experimental Study on Energy Release Mechanism and Crack Propagation Evolution of Sandstone under True Triaxial Loading. *Appl. Sci.* **2024**, *14*, 3655. [CrossRef]
11. Gu, L.; Zhao, J.; Zhou, Y.; Zhang, Y.; Wang, Z. Effect of stress difference and microfabric on the strength of deep granite. *Bull. Eng. Geol. Environ.* **2025**, *84*, 127. [CrossRef]
12. Zhang, X.; Zhao, J.; Jiang, M.; Xue, J.; He, B. Creep Failure Mechanism and Model of Granite under True Triaxial Loading and Unloading Conditions. *Int. J. Geomech.* **2024**, *24*, 06024015. [CrossRef]
13. Liu, Z.X.; Meng, X.R.; Zhao, G.M.; Zhang, R.F.; Liu, C.Y.; Kao, S.M.; Qi, M.J. Energy and damage analysis of sandstone under true triaxial compression. *Chin. J. Rock Mech. Eng.* **2023**, *42*, 327–341. (In Chinese)
14. Zhang, Q.H.; Meng, X.R.; Zhao, G.M. Energy Evolution and Fractal Characteristics of Sandstones Under True Triaxial Cyclic Loading and Unloading. *Fractal Fract.* **2024**, *8*, 714. [CrossRef]
15. Dong, C.; Fan, C.; Lu, X.; Zhao, G.; Qi, M.; Qin, R. Mechanical and Energy Evolution Characteristics of Sandstone under True Triaxial Cyclic Loading. *Appl. Sci.* **2023**, *13*, 7230. [CrossRef]
16. Cao, M.H.; Yang, S.Q.; Tian, W.L.; Huang, Y.H.; Li, Y. Experimental study on shear behavior of rough fractured granite under true triaxial monotonic and cyclic loading. *Int. J. Rock Mech. Min. Sci.* **2025**, *192*, 106164. [CrossRef]
17. Gong, H.; Wang, M.; Luo, Y.; Liu, T.; Fan, R.; Li, X. Stress-Confinement Effect on the Dynamic Mechanical Properties of Heterogeneous Granite Under Impact Loading: Experimental and Numerical Simulation. *Int. J. Numer. Anal. Methods Geomech.* **2025**, *49*, 633–653. [CrossRef]
18. Younessi, A.; Rasouli, V.; Wu, B. Sand production simulation under true-triaxial stress conditions. *Int. J. Rock Mech. Min. Sci.* **2023**, *7*, 130–140. [CrossRef]
19. Tiwari, R.P.; Rao, K.S. Numerical modeling of block mass model under triaxial compression. *Contrib. Rock Mech. New Century* **2004**, *1*, 1321–1326.
20. Zhang, C. Discrete Element Simulation of the Mechanical Propertiesof Granular Materials Under True Triaxial Stress. Master's Thesis, Beijing Jiaotong University, Beijng, China, 2021. (In Chinese)
21. Cundall, P.A. The Measurement and Analysis of Acceleration on Rock Slopes. Ph.D. Thesis, University of London, London, UK, 1971.
22. Cundall, P.A. A computer model for simulating progressive large-scale movements in blocky system. In *Proceedings of the Symposium of the International Society for Rock Mechanics*; International Society for Rock Mechanics and Rock Engineering: Lisbon, Portugal, 1971; pp. 129–132.
23. Cundall, P.A.; Strack, O.D.L. A discrete numerical model for granular assemblies. *Geotechnique* **1979**, *29*, 47–65. [CrossRef]
24. Zhang, L.; Wang, X.; Cong, Y.; Wang, Z.; Liu, J. Transformation mechanisms and criteria for static–dynamic failure of granite in a true triaxial unloading test. *Geomech. Geophys. Geo-Energy Geo-Resour.* **2023**, *9*, 104. [CrossRef]
25. Cao, M.H.; Yang, S.Q.; Tian, W.L.; Huang, Y.H.; Huang, M. Three-dimensional discrete element simulation of the triaxial cyclic loading of sandstone based on a nonlinear parallel-bonded stress corrosion model. *Comput. Geotech.* **2024**, *168*, 106167. [CrossRef]
26. Li, Y.P.; Zhang, Q.; Jiang, B.S. Numerical investigation on the fracture and mechanical behaviors of marble containing two parallel fissures under triaxial compression conditions using FDEM. *Theor. Appl. Fract. Mech.* **2024**, *131*, 104408. [CrossRef]
27. Li, Z.; Zhang, L.; Li, Q.; Cheng, H. Influence of loading rates under true triaxial stress on the mechanical properties and rockburst characteristics of granite. *Arab. J. Geosci.* **2021**, *14*, 2850. [CrossRef]
28. Chen, H.; Liu, L.; Zeng, P.; Yang, Y.; Zhang, T.; Liu, S.; Xia, S. The dynamic damage pattern and fine-scale damage characteristics of weathered granite after ore leaching. *Bull. Eng. Geol. Environ.* **2024**, *83*, 238. [CrossRef]
29. Peng, K.; Wu, T.; Liu, X.; Luo, K.; Luo, S.; Zhou, Z. Grain size effect on rockburst in granite: Evidence from true triaxial tests and grain-based numerical simulations. *Eng. Fract. Mech.* **2025**, *324*, 111253. [CrossRef]
30. Jing, W.; Cao, Z.; Jing, L.; Jin, R.; Rong, C. Crack Initiation and Propagation Mechanism of Flawed Rock Mass Based on Improved Maximum Distortion Energy Theory and PFC Numerical Simulation. *J. Fail. Anal. Prev.* **2024**, *24*, 1799–1813. [CrossRef]

31. Yang, W.M.; Geng, Y.; Zhou, Z.Q.; Li, L.C.; Ding, R.S.; Wu, Z.H.; Zhai, M.Y. True triaxial hydraulic fracturing test and numerical simulation of limestone. *J. Cent. South Univ.* **2020**, *27*, 3025–3039. [CrossRef]
32. Li, Y.; Zhang, Q.; Jiang, B. Numerical investigation on the mechanical and fracture behaviors of marble under cyclic loading and unloading true triaxial compression using discrete element method. *Comput. Part. Mech.* **2024**, *11*, 2753–2776. [CrossRef]

Disclaimer/Publisher's Note: The statements, opinions and data contained in all publications are solely those of the individual author(s) and contributor(s) and not of MDPI and/or the editor(s). MDPI and/or the editor(s) disclaim responsibility for any injury to people or property resulting from any ideas, methods, instructions or products referred to in the content.